Orientation bioprinting using microfibrous pore-forming bioinks for muscle tissue reconstruction

Debabrata Palai[1], Hana Yasue[1,2], Miho Ohta[1], Koichiro Uto[1], Tetsushi Taguchi[1], Akihiro Nishiguchi[1,2]*

[1] Biomaterials Field, Research Center for Macromolecules and Biomaterials, National Institute for Materials Science, 1-1 Namiki, Tsukuba, Ibaraki 305-0044, Japan
[2] Department of Materials Science and Technology, Graduate School of Advanced Engineering, Tokyo University of Science, 6-3-1 Niijuku, Katsushika-ku, Tokyo 125-8585 Japan

*Corresponding author: nishiguchi.akihiro@nims.go.jp

KEYWORDS: tissue reconstruction, liquid-liquid phase separation, 3D bioprinting, porosity, orientation

Abstract

Three-dimensional (3D) bioprinting provides a wide avenue for designing complex and customized constructs for regenerative medicine. Bioink formulations in 3D bioprinting usually lack micrometer-sized and interconnected pores for the supply of nutrients and oxygen and biological communications with host tissues, thus limiting cellular activities and therapeutic efficacy. Herein, we present microfibrous pore-forming bioinks for fabricating microporous hydrogels that encapsulate cells for muscle tissue reconstruction. Using phase separation technology, a liquid porogen was embedded into gelatin-based bioinks to form microfibrous structures. Printing bioinks with shear stress enabled the orientation of microfibrous pores along the printing direction, called orientation bioprinting, which facilitated the orientation of printed cells and enhanced myoblast differentiation. Moreover, the porous 3D scaffold exhibited promising results in terms of supplying nutrients and oxygen to improve cell survival. Printed tissue constructs were successfully transplanted into muscle tissue defects. This approach holds immense potential for creating anisotropic oriented 3D tissue constructs for applications in cell transplantation, drug screening, and disease modelling.

Introduction

Living tissues such as skeletal muscles, knee ligaments, tendons, and blood vessels have intrinsic structural features such as anisotropy and orientation [1–3]. In addition to biological cues, physicochemical structural features largely regulate functionalities, including mechanical properties, cell growth, and tissue regeneration [4–6]. Thus, material design to induce cell orientations in engineered scaffold is important for both 3D cell culture (in vitro) and therapeutic applications (in vivo) [7–9]. Several methods have been proposed for this purpose, including microfiber encapsulation [10,11], patterning [12,13], and stretching [14,15]. Recently, 3D bioprinting with extrusion, jetting, and lithography have garnered significant interest as an innovative tissue engineering approach for finely controlling 3D-cell position and tissue morphology [16–18]. In particular, 3D extrusion bioprinting enables the fabrication of 3D-tissue constructs with controlled cell densities and positions via layer-by-layer deposition based on a computer-aided design.

Bioink plays a crucial role in bioprinting, not only in controlling the quality of printed structures in terms of accuracy and shape fidelity, but also in providing biological, physical, and mechanical characteristics that control cellular activities and tissue regeneration [19]. Bioinks comprise the mixture of polymers (e.g. photocrosslinkable poly(ethylene glycol) (PEG), gelatin, dextran, and hyaluronic acid) and additives (e.g. nanoclay and photoinitiator) [20,21], which are chemically crosslinked to form mechanically stabilized hydrogels [22–24]. Hydrogels have been extensively used for bioprinting because of their biocompatibility, high water retention, and cell encapsulation capacity, which can mimic the microenvironment observed in natural tissues [25,26].

However, hydrogels often possess isotropic internal structures, and the encapsulated cells are not oriented. In previous studies to achieve cell alignment, the fabrication technique often embedded collagen or synthetic fibers during extrusion bioprinting [27,28]. Other techniques such as hydrogel microstrands [29] and stiffness patterning [30] have been designed in 3D-printing process and devices have also been developed [31,32]. However, these methods have number of drawbacks, such as, in case of fiber embedded bioink, the cell migration and remodeling often get inhibited if there is a mismatch between the fiber and hydrogel mechanical property. Moreover, fiber embedded gels or photocrosslinkable bioinks often lack perfusable microporosity, which causes poor nutrient diffusion and central necrosis. This motivates the development of new bio-inks which support cell aligning within printed construct and improve mass transport including oxygen, nutrients, and biomolecular signaling.

To improve mass transport and enhance cellular activity in stem cell–laden scaffolds, although nano-porous hydrogels have been engineered using PEG diacrylate and dextran where cells are typically encapsulated, the pores are too small for cells to migrate and infiltrate [33]. An alternative approach to generate microporosity involves liquid–liquid phase separation (LLPS) of gels. Specifically, integrating hydrogen-bonding moieties like ureidopyrimidinone (UPy) units into gelatin-based hydrogels induces phase separation, yielding injectable cell-delivery systems characterized by an interconnected network of micropores [34–36]. These studies demonstrate that microporosity can be achieved through spatiotemporally regulated covalent crosslinking in combination with selective phase dissolution, thereby facilitating improved material–tissue interactions and promoting efficient cellular integration. In this study, we developed microfibrous, pore-forming bioinks designed to enhance cell viability and alignment for skeletal muscle tissue reconstruction (Figure 1). Microporosity within the hydrogel matrix was achieved through the use of a liquid porogen based on LLPS technology. The bioink formulation consisted of ureidopyrimidinone (UPy)-modified gelatin (GUPy) and methacryloyl-modified gelatin (GelMA). Upon mixing, supramolecular interactions between UPy units facilitated phase separation, leading to the formation of a microporous GelMA-based hydrogel network. Application of shear stress during the extrusion-based bioprinting process induced alignment of the microfibrous pores along the printing direction—a process herein referred to as orientation bioprinting. The resulting anisotropic, microporous 3D scaffolds improved nutrient and oxygen transport, thereby enhancing cellular survival and promoting cell orientation. This facile and scalable approach to fabricating structurally anisotropic tissue constructs holds significant promise for applications in tissue engineering and regenerative medicine.

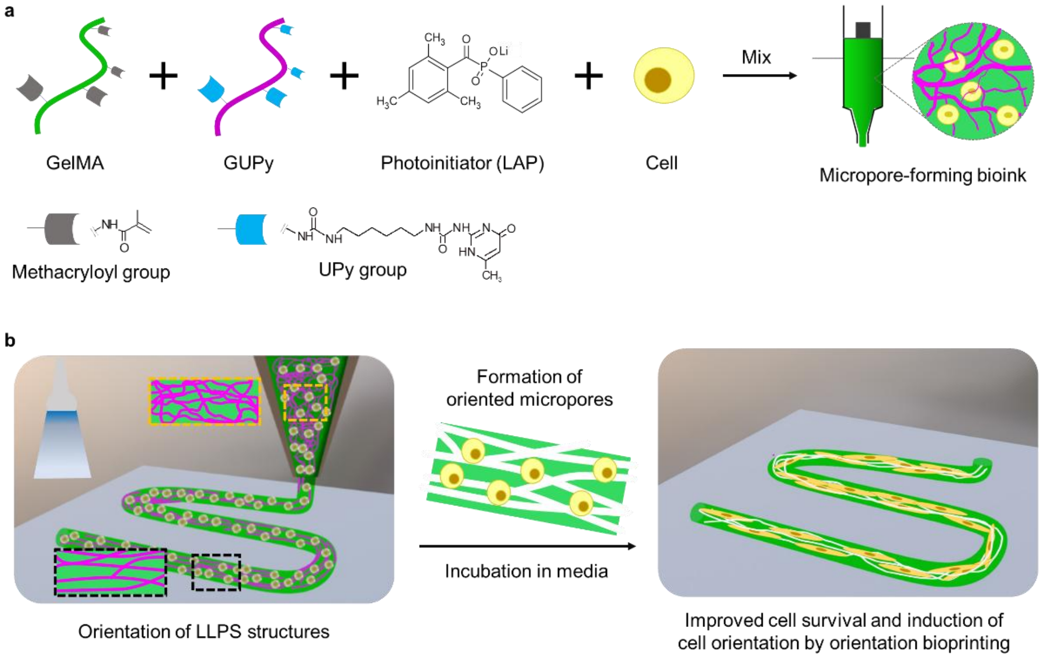

Figure 1. Schematic presentation of (a) preparation of bioink encapsulated with myoblast cells and porogen. (b) The printing of 3D cell-laden construct, microporosity formation, and oriented cell proliferation.

2. Materials and methods

2.1. Materials: Porcine skin-derived gelatin (sG, M_w: 140 kDa), 2-amino-4-hydroxy-6-methylpyrimidine, RPMI1640 medium, pepsin, fetal bovine serum (FBS), fluorescein isothiocyanate, lithium phenyl-2,4,6-trimethylbenzoylphosphinate (LAP), and methacrylic anhydride (MAA) were purchased from Sigma-Aldrich (USA). The 2,4,6-trinitrobenzenesulfonic acid sodium salt dihydrate (TNBS) and 1,6-diisocyanatohexane were purchased from Tokyo Chemical Industry Co., Ltd. (Japan). Phosphate-buffered saline (PBS) was purchased from Nacalai Tesque Inc. (Japan). *N*-hydroxysuccinimide (NHS)-tethered Cy5.5, was purchased from Lumiprobe (USA). Penicillin/streptomycin (P/S), trypsin, rhodamine-labelled phalloidin, 4′,6-diamidino-2-phenyl-indole (DAPI), and anti-goat IgG antibody conjugated with Alexa Fluor 488 (Invitrogen) were purchased from Thermo Fisher Scientific (USA). Amikacin solution was purchased from Meiji Seika Pharma (Japan). Dialysis membranes (molecular weight cut-off (MWCO) value: 12–14 kDa) were purchased from Repligen (USA). Dimethyl sulfoxide (DMSO), sodium carbonate, sodium bicarbonate, peracetic acid, and bovine serum albumin (BSA) were purchased from Fujifilm Wako (Japan). The mouse myoblast cell line (C2C12 cell) was purchased from the European Collection of Authenticated Cell Cultures (ECACC). Green fluorescence protein (GFP)-expressing C2C12 cells were purchased from Cellomics Technology (USA). C57BL/6 mouse bone marrow-derived mesenchymal stem cells (MSC) were purchased from Cyagen (USA). MSC growth medium (MesenCult Expansion Kit for mouse) was purchased from Veritas (Japan). Anti-myosin heavy chain (MHC) antibodies were purchased from R&D Systems Inc. (USA). The WST-8 assay kit was purchased from DOJINDO (Japan). Cytoplasmic membrane dye (DiI, CellBrite®) was purchased from Biotium (USA).

2.2. Synthesis of GelMA and GUPy GelMA was synthesized as previously described [37]. sG (10 g, 10 wt%, amino group: 290 µmol/g) was dissolved in 0.25 M carbonate-bicarbonate buffer (100 mL, pH = 9) at 50 °C. MAA (3.25 mmol, 492.3 µL) was added to the gelatin solution with magnetic stirring. The reaction proceeded for 1 h at 50 °C, and then the pH was readjusted to 7.4 to stop the reaction. The products were dialyzed in pure water for 3 d and freeze-dried to obtain GelMA. The degree of substitution (D.S.) of MA with gelatin was determined using TNBS. The UPy derivative and GUPy were synthesized according to a previous report [38]. Briefly, UPy unit was synthesized via the reaction of 2-amino-4-hydroxy-6-methylpyrimidine (33.0 mmol; 4.1 g) with 1,6-diisocyanatohexane (148.6 mmol; 25.0 g). After the reaction at 100 °C for 16 h with stirring, the product was obtained by precipitating and washing with hexane and collecting via filtration. UPy units (38.6 mg, 0.132 mmol, 50 mol% equivalent to amino groups in gelatin) were then dispersed in DMSO (5 mL) and added to gelatin solution (1 g) in DMSO (20 mL) at 50 °C with stirring. The reaction was continued for 24 h at 25 °C with stirring. The product was obtained by precipitation in cold ethanol and ethyl acetate (v/v = 1/1) with stirring. The precipitate was collected using a glass filter and washed with cold chloroform and ethanol. The products were dried at 25 °C under reduced pressure. The D.S. of the UPy units in the obtained samples was quantified using UV spectroscopy.

2.3. Synthesis of GelMA-fluorescein, GUPy-Cy5.5: GelMA-FITC and GUPy-Cy5.5 were synthesized according to a previous report [34]. Briefly, sG was dissolved in CB buffer and the MAA solution was added in the same manner as that for GelMA synthesis. FITC (2 mol% equivalent to the amino groups in sG) dissolved in 1 mL of DMSO was slowly added to the solution. The reaction was continued at 50 °C for 1 h in the dark. The pH of the solution was adjusted to 7.4 and dialyzed in ultrapure water for 3 d in the dark. GelMA-FITC was obtained by freeze drying. To synthesize GUPy-Cy5.5, sG (1 g) was reacted with the UPy derivatives in the same manner as that described for GUPy synthesis. After 5 h with stirring, NHS-tethered Cy 5.5 (1.07 mg, 1.5 μmol) dissolved in DMSO was added to the solution and stirred for 24 h at 25 °C. The final product was washed, dried, and collected as described in the previous section.

2.4. Preparation of bioinks: LAP (0.01 wt%) was dissolved in PBS at 25 °C. GelMA (10 wt%), GUPy (12 wt%), and unmodified gelatin (12 wt%) were dissolved in LAP-PBS solution at 50 °C with stirring. The dissolved solutions were stored at 37 °C until used. Solutions of GelMA and GUPy were mixed vigorously at equal volumes using a pipette to prepare the pore-forming bioinks (GelMA+GUPy). As a control, a nonpore-forming bioink was prepared by mixing GelMA with unmodified gelatin. The LLPS structure of the fluorescently labelled gelatin derivative was visualized under a confocal laser scanning microscope (CLSM; LSM 900 with Airyscan2, Zeiss, Germany).

2.5. Rheological measurement: Rheological measurements were performed using a rheometer (MCR301, Anton Paar GmbH, Austria) equipped with a jig with a diameter of 10 mm. To measure the viscosity of bioinks, nonporous and pore-forming bioinks were placed onto a stage of rheometer and steady rate sweep within shear rate 0.01–1000 s^{-1} was conducted at 37 °C. To evaluate the storage modulus (*G*’) of crosslinked hydrogels, nonporous and pore-forming bioinks were placed onto a silicone mold (circular disc: 10-

mm diameter and 1-mm thickness) and crosslinked under UV exposure (405 nm, 40 s) using BIO X (BICO, Sweden). Engineered nonporous and porous hydrogels were then immersed in PBS overnight at 37 °C. Excess PBS was carefully cleaned from the surface of hydrogel discs using paper towel and placed on the stage of the rheometer (prewarmed to 37 °C). The gap between the sample and jig was set to 0.5 mm until a neutral sensor force was observed. To measure *G*' of hydrogels, frequency sweep test was performed from 0.1 to 100 rad/s at 1% strain, which was within linear viscoelastic region. The *G*' of nonporous and porous hydrogels were evaluated by averaging shear modulus at 5 rad/s from frequency sweep tests.

2.6. Swelling behavior of hydrogels: To measure the swelling ratio of the nonporous and porous hydrogels, photocrosslinked cylindrical hydrogels with a diameter of 10 mm and height of 2 mm were prepared. The samples were completely immersed in 10 mL PBS and incubated at 37 °C for 24 h. Finally, the swollen weight of each sample was recorded (W_s) after gently removing the excess PBS from the surface of the sample using filter paper. The samples were freeze-dried at reduced pressure, and the dry weight was recorded (W_d). The swealing ratio was calculated as ((W_s-W_d)/W_d).

2.7. 3D printing and quality check: Tinker CAD (Autodesk Inc., USA) was used to design the 3D models; star shape, grid structure, parallel line tissue construct, with the built-in Slic3r software used for layering. To perform 3D-printing using an extrusion-based 3D bioprinter, the bioink was extruded using a blunt needle (25 G). Using the printing conditions (temperature, printing speed, and extrusion pressure) mentioned in Table 2, 3D structures with five layers of grid structure with dimensions of 20 × 20 × 1 mm^3 and line tissue constructs of 20 × 9.6 × 1 mm^3 were obtained. In all printed structures, a grid infill pattern was used. To print the multilayered structure, the extrusion pressure was increased by 5 kPa/layer as the viscosity of the ink gradually increased during the printing process. To crosslink the printed 3D structures, each layer of the structure was exposed to UV light (405 nm) from a distance of 6 cm for 40 s.

The printing quality of the 3D structure was evaluated in terms of printability parameter (Pr) and structural uniformity by measuring the fluorescence intensity horizontally. A grid structure (20 × 20 × 1 mm^3) was prepared and printed using a 3D bioprinter. After printing each construct, at least three printed structures were observed and analyzed using the ImageJ software to calculate the pore area, perimeter, and Pr. The Pr value was calculated using the following equation as previously described [39].

$$Pr = {L^2}/{16A} \tag{2}$$

where, "L" is the perimeter and "A" is the area of the square mass of the grid structure.

To measure the stacking uniformity of the layer, the grid structures were imaged using CLSM. The fluorescence intensity of each strand of the grid structure was quantified using a built-in processing software. The porosity of the hydrogels after incubation in PBS was analyzed from the CLSM images of hydrogels with fluorescently labelled gelatin using the ImageJ software.

2.8. Cytocompatibility test: C2C12 cells were cultured in RPMI-1640 medium supplemented with 10% FBS and 1% P/S. MSCs were cultured in MSC growth medium. The cells were incubated at 37 °C and 5% CO_2, with the media replaced at 48 h intervals. C2C12 cells (1 × 10^4/well) were seeded in 96-well plates and cultured for 24 h at 37 °C and 5% CO_2. The cells were then exposed to the GelMA solution for another 24 h. The number of cells was counted using the WST-8 assay. Briefly, 10 µL of WST-8 reagent was added to 100 µL of culture medium and incubated for 2 h. The absorbance of the medium was monitored at 450 nm using a microplate reader and the cell number was quantified by plotting a standard curve. The absorbance of cells cultured in the medium was set to 100%.

2.9. 3D bioprinting using pore-forming bioinks: Bioinks were filtered using a 0.22-µm syringe filter for sterilization. C2C12 cells or MSCs were collected via trypsin treatment and centrifugation at 1200 rpm for 5 min at 4 °C. The bioink (total volume: 1 mL) and cells (2×10^7 cells) were mixed in Eppendorf tubes using a pipette. Using a 1-mL sterilized syringe and a female Luer lock adapter (BICO, Sweden), the bioink was transferred to a 3-mL sterilized cartridge for 3D printing. Printing was performed using a low-cell-attachment Petri dish (35 mm) as described above. Printed cell-laden structures were rinsed once with the culture media and incubated for 3 d at 37 °C and 5% CO_2. For the differentiation of C2C12-printed tissues, the cell-laden structure was cultured in RPMI1640 supplemented with 10% FBS and 1% P/S for 3 d at 37 °C and 5% CO_2. After 3 d, the culture medium was replaced with DMEM supplemented with 2% horse serum and 1% P/S and cultured for another 7 d. The medium was replaced with fresh medium every 48 h.

2.10. Cell trajectories inside the 3D structure: GFP-expressing C2C12 cells were used to measure cell trajectories. Cell-laden line structures ($20 \times 0.1 \times 1$ mm^3, 5×10^6 cells/mL) were printed and cultured in media for 24 h. The trajectory of cells was captured at 5 min intervals for 24 h while incubating at 37 °C and 5% CO_2 in a CLSM chamber system. The velocity and trajectory of cell movement in the nonporous and porous structures were analyzed using the ImageJ software.

2.11. Cell viability assay in hydrogels: A cell-laden line structure (line structure, four layers; C2C12: 20 × 10^6 cells/mL) was printed and crosslinked using UV light. The live/dead assay was conducted using a Live/Dead Cell Staining Kit II (Promokine, PromoCell, Germany) according to the manufacturer's protocol. Briefly, the cell-laden structure was cultured in RPMI1640 medium for 1 d at 37 °C and 5% CO_2. The cell-laden structure was rinsed twice with PBS to remove the serum esterase activity. Dye solutions were thawed at 25 °C and a 4-mL aliquot (2 μM Calcein-AM, 4 μM EthD-III,) was prepared in PBS. The dye (3 mL) was then added to the cell-laden hydrogel structure and incubated for 30 min at 25 °C. The sample was rinsed with PBS once, and images of live (green, calcein) and dead (red, EthD-III) cells in various locations within the 3D construct were obtained using CLSM. The cell viability was calculated by dividing the total number of live cells by the total number of cells (live and dead).

2.13. Immunostaining and orientation quantification: The printed cell-laden structures were washed with PBS and fixed with 4% paraformaldehyde for 1 h. After washing with PBS, the cells were permeabilized with 0.2% Triton-X for 30 min. After washing the sample thrice with PBS, the cells were blocked with 1% BSA/PBS for 1 h. Cells were stained with rhodamine-labelled phalloidin (1:100) and anti-MHC (1:100) overnight at 4 °C. After washing with PBS, the samples were immersed overnight in anti-goat IgG antibody conjugated with Alexa Fluor 488 (1:500). After washing with PBS, cells were stained with DAPI for 1 h at 25 °C. Cell morphology was observed using CLSM. The area of the cells, fiber diameter, and fusion index of the differentiated cells were quantified using the ImageJ software. To quantify the orientation of the differentiated myotubes in the 3D structure, the acquired images were analyzed using the OrientationJ plugin (version 2.0.7, BIG; EPFL, Switzerland) in ImageJ. The histogram of oriented myotubes was plotted in a polar stem plot between 90° to -90° using matplotlib.

2.14. Transplantation to VML models: All animal experiments were approved by the Animal Care and Use Committee of the National Institute for Materials Science (No: 80-2024-1). To prepare the cell-laden 3D printed structure, MSCs were labelled with fluorescent lipophilic DiI, according to the manufacturer's protocol. Briefly, MSCs were collected using trypsin, and cell pellets were suspended in RPMI medium (serum-and P. S-free) at a density of 1×10^6 cells/mL. Cell labelling solution was added to the suspension solution (5 µL to 1 mL cell suspension) and incubated at 37 °C for 20 min. The collected cell pellets were washed with PBS. After removing the supernatant, the cells were mixed with sterilized pore-forming bioink for 3D printing. Cell-laden constructs (line structure, $5 \times 0.1 \times 1$ mm^3) were made using Dil-labelled MSCs (1×10^7 cells/mL). Mice (6–8 week-old female BALB/c nude mice; Jackson Laboratory, USA) were anesthetized by inhalation of 2% isoflurane. The dorsal surfaces of the mice were aseptically prepared using 70% ethanol. Volumetric muscle defects were induced in the hind limbs of mice. An incision was made along the anterior aspect of the hind limb to expose the tibialis anterior (TA) muscle and a defect ($5 \times 2 \times 2$ mm^3) was made. All mice were intraperitoneally administered amikacin (1 mg/kg). To observe cell engraftment, tissue constructs of DiI-labelled MSCs were transplanted into the defect. The mice were euthanized by exsanguination 7 d posttransplantation. The tissues were collected and fixed in 10% formalin buffer solution and stained with DAPI for CLSM observation.

2.15. Statistical analysis

The results are expressed as the mean ± SD. One-way ANOVA followed by Tukey's multiple comparison post-hoc test was used to assess differences among groups. Experiments were repeated multiple times as independent experiments. The data shown in each Figure are a complete dataset from one representative independent experiment. None of the samples were excluded from the analysis. Statistical significance is indicated as $*P < 0.05$, $**P < 0.01$, $***\ P < 0.001$, and $****P < 0.0001$. Statistical analyses were performed using the GraphPad Prism software (version 8.0; GraphPad Software, USA).

3. Results and Discussion

3.1. Bioinks preparation and 3D printing parameters

Pore-forming bioinks with LLPS structures were prepared by mixing equal volumes of 10 wt% GelMA and 12 wt% GUPy. GelMA with 71% D.S. and GUPy with 48% D.S. were synthesized. CLSM observations showed that GUPy formed LLPS structures when mixed with GelMA, and the obtained LLPS structures were similar to the previously reported microfibrous network structures [34] (Figure 2a). For extrusion-based bioprinting, the bioinks must exhibit adequate zero-shear viscosity and shear-thinning properties. Pore-forming bioinks possessed higher viscosity compared with nonpore-forming bioinks owing to strong hydrogen bonding between UPy units and showed shear thinning property, which is desirable for extrusion bioprinting (Figure 2b). To characterize the mechanical properties of the hydrogels, the pore-forming bioinks were crosslinked by UV exposure to form porous hydrogels. The storage modulus (*G*') of nonporous and porous hydrogels was almost the same within the linear elastic region (Figure 2c). The swelling ratio of the nonporous and porous hydrogels was 14.1 and 8.9, respectively.

For 3D printing using pore-forming bioink, bioink extruded was deposited on a substrate kept at 12 °C, which is below the gelation temperature of GelMA and GUPy, and underwent physical crosslinking. This instant gelation helped retain its shape until the chemical crosslinking of GelMA by UV exposure. Several printing parameters (printing speed and extrusion pressure) were determined to investigate the printability of the structures (Figure 2d). The diagram indicated that the range shown in the green area was suitable for printing conditions, whereas high extrusion pressure (>48 kPa), low printing speed (< 10 mm/s), low extrusion pressure (<20 kPa), and high printing speed (>15 mm/s) resulted in over- or underextrusion, respectively. The concentration ratio of GelMA to GUPy affected the printability and Pr. The value of the higher GUPy ratio was close to 1, which is suitable for printing [39] (Figure 2e). This is because the GUPy-rich phase formed intramolecular hydrogen bonds and improved the viscosity of the bioinks.

Based on the optimization of the extrusion pressure, printing speed, and printability, 3D grid structures were printed using the parameters listed in Table 1. Often, when printing 3D structures with multiple layers, the intersecting filaments diffuse because of the accumulation of bioink, and the height of the scaffold decreases in the z-direction because of gravitational force. This compromises the stacking efficiency of the layers and fidelity of the 3D structure. Following a previously reported procedure [39], the stacking efficiency of the grid structure was measured by quantifying the fluorescence intensity of the 3D image from horizontal scanning using CLSM (Figure 2f, g). The intensity profile revealed that the printed layers were uniformly stacked. Complex structures with eight layers were printed under the same conditions (Figure S1a). The printed 3D structures were stable and maintained their shape for 8 d in PBS at 37 °C (Figure S1b).

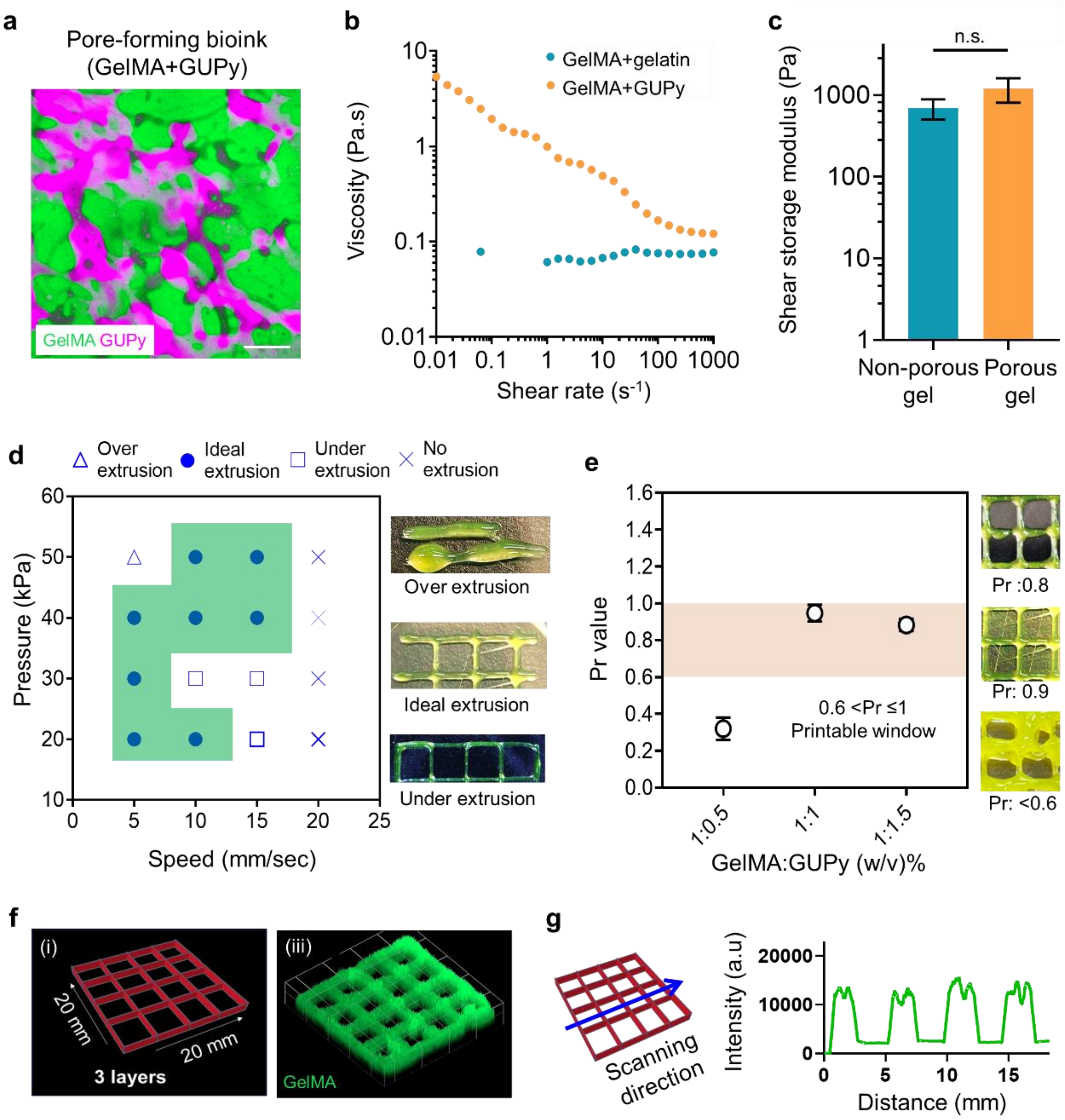

Figure 2. (a) CLSM images of pore-forming bioink composed of GelMA and GUPy. For the visualization, GelMA-FITC (green) and GUPy-cy 5.5 (violet) were used. (b) Viscosity of nonporous and pore-forming bioink under shear rates from 0.01 to 1000 s^{-1}. (c) Shear storage modulus of nonporous and porous hydrogels ($n = 3$). (d) Diagram of the appropriate combination (green) of printing parameters for ideal extrusion of LLPS bioink. (e) Printability factor (Pr) analysis of the bioink as per the combinations of GelMA/GUPy concentration. (f) Design and CLSM image of printed grid structure. (g) Horizontal line scan profile of printed structre's layer from CLSM image. Data are presented as the mean ± S.D. n.s. denotes not significant, analyzed using the two-tailed Student's *t*-test. Scale bar represents 50 μm.

Table 1. Parameters for 3D printing.

GelMA concentration	GUPy concentration	Extrusion pressure	Print head temperature	Print bed temperature	XY plotting speed	UV light intensity	UV exposure time	Nozzle inner diameter	Exposure distance
(w/v)	(w/v)	(kPa)	(°C)	(°C)	(mm/min)	(nm)	(s)	(mm)	(cm)
10	12	45–65	32	12	12-15	405	40	0.25	6

3.2. Pore formation and orientation through the combination of LLPS and 3D printing

Hydrogels often possess dense polymer network structures with no micropores, which may limit the supply of nutrients and oxygen and restrict the survival of encapsulated cells [10,33,40]. Phase separation is useful for introducing porous structures into hydrogels [41,42], and several studies have demonstrated the bioprinting of porous hydrogels . However, these methods were not successful in fabricating interconnected pores or three-dimensional enough void spaces. We aimed to introduce interconnected microfibrous pores into bioprinted hydrogels using hydrogen-bonding-driven LLPS. Two-layered grid structures (20 × 20 mm) were printed using a pre-sheared LLPS bioink without cells (Figure 3a). The printed structure exhibited good shape retention, and microfibrous capillary networks composed of GUPy were observed. After incubating the hydrogels in PBS for 24 h, porous structures were formed in 3D printed hydrogels due to the dissolution of GUPy as a liquid porogen (Figure 3b). The porosity of 3D printed structure was approximately 30%, whereas no micropores were observed in the hydrogels from the nonpore-forming bioink, in consistency with our previous report [34] (Figure 3c). Micropores in 3D printed hydrogels may serve as channels to enhance the mass transport of nutrients and oxygen, thereby improving cell survival inside the hydrogels.

To evaluate the orientation of the LLPS structures and micropores, the structural orientation of the porous hydrogels induced by applying shear stress (shear stress by printing) or by dropping a pregel onto a substrate (no shear stress) was compared (Figure 3d). To align micropores in printed structures, the shear strain ($\dot{\gamma}$) was applied to the bioink at 981 s^{-1} (Supplementary Information). To visualize and quantify the directionality an orientation analysis was conducted using minimum three different printed structures and polar stem plot revealed that applying shear stress to the bioinks facilitated the orientation of the phase-separated GelMA hydrogels along the printing direction, whereas hydrogels prepared without shear stress possessed random configurations (Figure 3e). This result indicated that 3D printing is useful for aligning LLPS structures by applying optimal shear stress with a controlled printing speed and pressure. Hydrogel-embedded fibers were aligned when shear stress was applied using 3D-printing [28]; likewise, viscous LLPS microstructures can be aligned by shear stress along the printing direction. This combined approach of LLPS and 3D printing not only provides micropores for cell survival but also enables the unidirectional orientation of cell-adhesive voids for cell orientation.

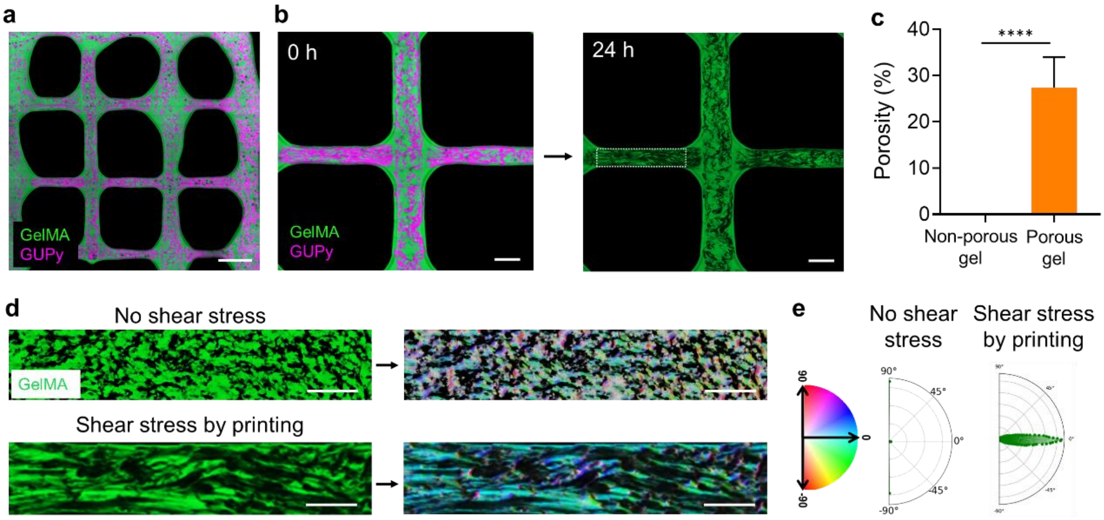

Figure 3. (a) CLSM image of a 3D-printed structure. GelMA-FITC and GUPy-Cy5.5 were used for visualization. (b, c) Micropores were formed after immersion in PBS for 24 h. Porosity was analyzed from CLSM images after immersion in PBS (n = 6). (d) Orientation analysis of porous hydrogels prepared by dropping pore-forming bioink on substrate (no shear stress) and by printing with shear stress application. (e) Represents the polar plot of the distribution of oriented porous structure by using shear stress. Data are presented as the mean ± SD. $****P < 0.0001$, analyzed by the two-tailed Student's *t*-test. Scale bars represent 2 mm for (a), and 1 mm for (b), 500 μm for (d), respectively.

3.3. Orientation bioprinting of myoblast cells

To design 3D cell-laden constructs using bioink, addressing some important factors such as the effects of printing conditions (shear force, UV exposure, and toxicity of GelMA) on cell viability is necessary. The cytotoxicity assay showed that GelMA was highly cytocompatible with mouse myoblasts (Figure S2). Owing to the gelation property and the presence of cell-adhesive motifs in GelMA, this approach effectively localized cells within the scaffold and minimized cell loss during the subsequent selective dissolution of the porogen phase. Myoblast cells were encapsulated in nonporous and porous hydrogels to evaluate cell adhesion. CLSM observations showed that the porous hydrogels substantially enhanced cell adhesion and spreading, whereas almost all cells were round in the nonporous hydrogels after 3 days of incubation (Figure 4a). Quantitative analysis of cell motility, combined with trajectory tracking, revealed that the cell migration velocity of myoblasts encapsulated within microporous hydrogels was approximately 2.6 times higher than that observed in non-porous hydrogels. (Figure 4b and Figure S3). Moreover, the live/dead staining assay revealed that many viable myoblast cells were present in the porous hydrogels compared with those in the nonporous hydrogels, where some cells were dead (Figure 4c,d). Although GelMA is known for its cytocompatibility, the photocrosslinked mixtures of GelMA and non-porogen results in dense hydrogel networks with no micropore which may restrict cell migration, diffusion of nutrients, and oxygen. In the living body, nutrients and oxygen are supplied from blood capillaries within a distance of 200 μm from cells [43], with poor mass transport causing hypoxia and necrosis [44]. Microfibrous pores in the hydrogels facilitated mass transport to improve cell survival, whereas nonporous hydrogels suppressed the diffusion of nutrients and oxygen (Figure S4).

Next, the effects of the microporous structures of the hydrogels on myotube formation were investigated. Simple line structures were printed using bioinks to form myoblast constructs in nonporous and porous hydrogels. After the differentiation of myoblast cells, cellular differentiation was evaluated using MHC staining, which is a marker for identifying skeletal muscle tissue differentiation and maturation. CLSM observation of differentiated tissue constructs showed that myoblast cells in porous hydrogels formed thick myotubes, whereas few cells were MHC-positive and no myotubes were formed in nonporous hydrogels (Figure 4e). Quantitative analysis of the myotube diameter (indicative of the quality of myoblast cell differentiation and maturation) and fusion index (the ratio of nuclei in MHC-stained myotubes to total nuclei) revealed an improvement in the differentiation and maturation of myoblast cells in the porous hydrogels (Figure 4f,g). Previous reports suggested that a hydrogel micropatterned with grooves <50 μm promoted C2C12 myotubes maturation by enhancing sarcomere formation [45,46]. As porous hydrogels possess micropores smaller than 50 μm, spatially restricted fiber-shaped voids may be favorable for the differentiation of myoblast cells. To confirm the degree of alignment of mature myotubes, unidirectionally aligned fiber structures were printed using pore-forming bioinks. From the results of the color pattern and polar stem distribution plot obtained from actin- and MHC-stained CLSM images, we noted that 3D printed myoblast cells in porous hydrogels were aligned along the printing direction, which may facilitate the differentiation and maturation of encapsulated cells and muscle cells infiltrating from host tissues (Figure 4h). These observations suggested that orientation bioprinting using LLPS bioinks not only provides a microporous scaffold to improve cell spreading, migration, and survival but also accommodates unidirectionally oriented printed cells, which may contribute to the regeneration of injured muscle tissues.

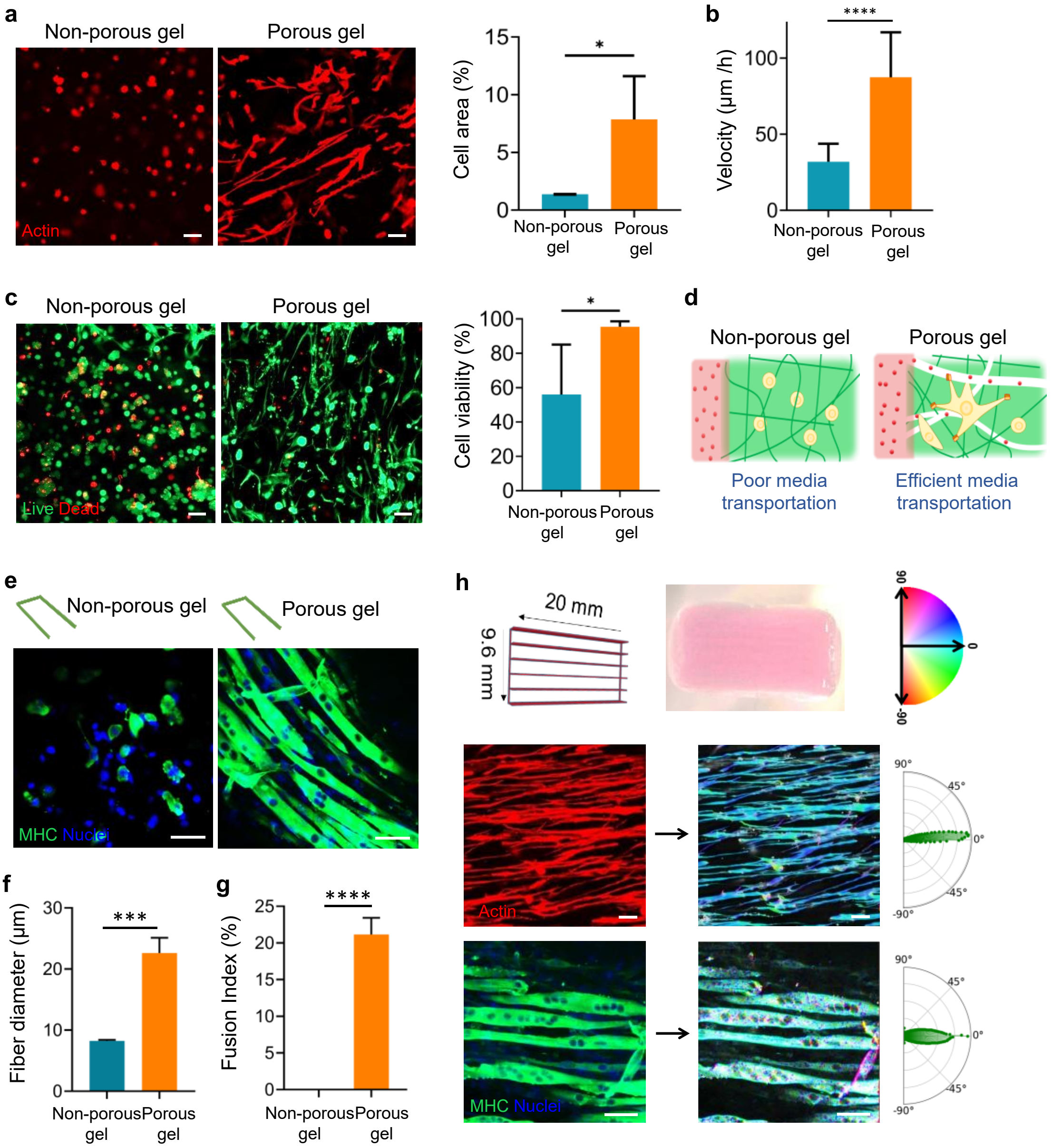

Figure 4. (a) CLSM images of encapsulated myoblast cells in printed nonporous and microporous hydrogels. GelMA-FITC (green) was used to visualize hydrogels, and actin was stained with phalloidin (red), and relativerea of adherent cells in nonporous and porous gels (n = 3). (b) The velocity of GFP-expressing myoblast cells in nonporous and porous hydrogels analysed for 24 h (n = 3). (c) Live/dead stained images of cells in hydrogels. Live and dead cells were stained with calcein (green) and EthD-III (red), respectively (n = 3). (d) Schematic of media diffusion and cell migration inside hydrogels. (e) Differentiation of myoblasts in droplet hydrogel (porous) and printed hydrogels (nonporous and porous) for 7 d. Cells were stained with MHC antibody (green) and DAPI (blue). (f,g) Quantitative analysis of fiber diameter and fusion index of differentiated cells in hydrogels (n = 3). (h) CLSM images, color pattern, and polar stem distribution plot of differentiated myoblasts in printed porous hydrogels. The actin and nuclei were stained

with phalloidin (red) and DAPI (blue), respectively. MHC was stained using MHC (green). Data are presented as the mean ± S.D. *$P < 0.05$, ***$P < 0.001$, ****$P < 0.0001$, analyzed using the two-tailed Student's *t*-test. Scale bars represent 50 μm.

3.5. Transplantation of engineered tissue constructs

To address whether engineered tissue constructs can be transplanted into living tissues, MSCs were printed using micropore-forming bioinks to create 3D printed MSC constructs and transplanted into mouse VML models. MSCs were used as donor cells because they are clinically available for regenerative medicine approaches [47]. As a tissue defect model, VML mice, which are known to have severe traumatic injuries in skeletal muscles, were used in this study. VML defects (5 × 2 × 2 mm) were created in the TA muscle of mice, and the engineered MSC constructs were transplanted into the defects soon after printing, without further culture (Figure 5a). Prior to transplantation, the adhesion of MSCs to the porous hydrogels was confirmed (Figure 5b). CLSM observations showed that MSCs adhered to and spread in the hydrogels, as observed in the case of the encapsulation of myoblast cells, indicating that porous hydrogels can support the adhesion of MSCs. Next, the graft survival of the transplanted cells against VML was evaluated. DiI-labeled MSCs were printed and transplanted into VML defects. Transplanted tissues were retained at the defect site 7 d after transplantation (Figure 5c). CLSM images of DiI-MSC revealed that cells were efficiently grafted to the defects (Figure 5d, e). These results suggested that engineered tissue constructs can be delivered and grafted onto host tissues without specific fixation procedures. We expect that this method can be used to regenerate muscle tissue defects through paracrine signaling from transplanted MSC constructs.

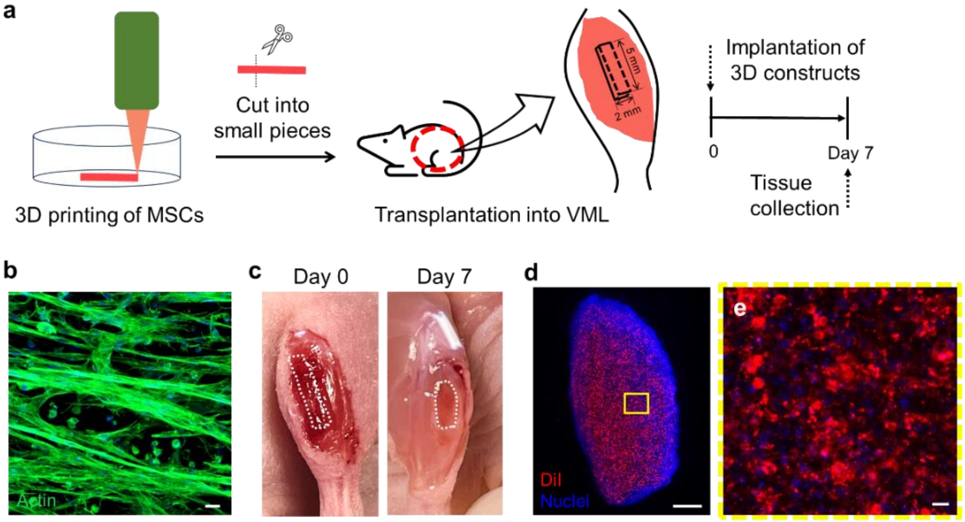

Figure 5. (a) Schematic of the procedure of transplantation of 3D-printed MSC constructs. (b) CLSM image of 3D-printed MSC constructs after 1 d of incubation in vitro. Actin was stained with phalloidin (green). (c) Photos of VML in TA muscle at day 0 and 7 after transplantation of the 3D-printed MSC construct. (d) CLSM images of TA tissues at 7 d after transplantation. MSCs were fluorescently labeled with DiI and nuclei were labelled with DAPI (blue). Scale bars represent 20 μm for (b, e) and 500 μm for (d).

Conclusion

In conclusion, this study demonstrated 3D anisotropic muscle tissue constructs fabricated by orientation bioprinting using LLPS bioinks. Systematic optimization of the extrusion parameters was performed to enhance printability. Microfibrous pore-forming bioinks composed of GelMA and GUPy possessed the shear-thinning property required for 3D extrusion bioprinting. UV-cross-linked porous hydrogels exhibit the necessary mechanical properties and biodegradability for use as regenerative materials. Interconnected microporous structures were formed in the hydrogels, and these pores were unidirectionally oriented because of the applied shear stress during the printing process. These anisotropically oriented microporous structures remarkably improved the inward diffusion of nutrients and oxygen, resulting in a notable enhancement in cell survival, spreading, migration, and differentiation compared with nonporous hydrogels. The cell-laden structure of the LLPS bioink could be transplanted into VML mouse models. This straightforward strategy improves therapeutic applications and has the potential to significantly affect applications in regenerative medicine, drug screening, and disease modelling.

Data availability statement

The data cannot be made publicly available upon publication because no suitable repository exists for hosting data in this field of study. The data that support the findings of this study are available upon reasonable request from the authors.

Acknowledgements

This work was supported by funds from the Japan Society for the Promotion of Science (JSPS) KAKENHI (grant no. 22H03962), Inamori Foundation, Toshiaki Ogasawara Memorial Foundation, and Uehara Memorial Foundation.

Conflict of Interest

The authors declare no conflicts of interest.

References

[1] Datta P, Vyas V, Dhara S, Chowdhury A and Barui A 2019 Anisotropy properties of tissues: a basis for fabrication of biomimetic anisotropic scaffolds for tissue engineering J *J. Bionic Eng* **16** 842–68

[2] Mondrinos M J, Alisafaei F, Yi A Y, Ahmadzadeh H, Lee I, Blundell C, Seo J, Osborn M, Jeon T-J, Kim S M, Shenoy V B and Huh D 2021 Surface-directed engineering of tissue anisotropy in microphysiological models of musculoskeletal tissue *Sci. Adv.* **7** eabe9446

[3] Takahashi R, Wu Z L, Arifuzzaman M, Nonoyama T, Nakajima T, Kurokawa T and Gong J P 2014 Control superstructure of rigid polyelectrolytes in oppositely charged hydrogels via programmed internal stress *Nat. Commun.* **5** 4490

[4] Qu F, Li Q, Wang X, Cao X, Zgonis M H, Esterhai J L, Shenoy V B and Mauck H L 2018 Maturation state and matrix microstructure regulate interstitial cell migration in dense connective tissues Sci *Sci. Rep* **8** 1–13

[5] Peng R, Yao X and Ding J 2011 Effect of cell anisotropy on differentiation of stem cells on micropatterned surfaces through the controlled single cell adhesion Biomaterials *Biomaterials* **32** 8048–57

[6] Palai D, Yasue H, Ito S, Komatsu H, Taguchi T and Nishiguchi A 2025 Functionalization of viscoelastic gels with decellularized extracellular matrix microparticles enhances tissue adhesion, cell spreading, and tissue regeneration *Biomater. Sci.*

[7] Leijten J 2017 Spatially and temporally controlled hydrogels for tissue engineering Mater *Sci. Eng. R* **119** 1–35

[8] Vo J, Mastoor Y, Mathieu P S and Clyne A M 2021 A simple method to align cells on 3D hydrogels using 3D printed molds Biomed *Biomed. Eng. Adv* **1** 100001–25

[9] Li Y, Huang G, Zhang X, Wang L, Du Y, Lu T J and Xu F 2014 Engineering cell alignment in vitro *Biotechnol. Adv.* **32** 347–65

[10] Shao L, Hou R, Zhu Y and Yao Y 2021 Pre-shear bioprinting of highly oriented porous hydrogel microfibers to construct anisotropic tissues *Biomater Sci* **9** 6763–71

[11] Onoe H, Okitsu T, Itou A, Kato-Negishi M, Gojo R, Kiriya D, Sato K, Miura S, Iwanaga S, Kuribayashi-Shigetomi K, Matsunaga Y T, Shimoyama Y and Takeuchi S 2013 Metre-long cell-laden microfibres exhibit tissue morphologies and functions *Nat. Mater.* **12** 584–90

[12] Wade R J, Bassin E J, Gramlich W M and Burdick J A 2015 Nanofibrous hydrogels with spatially patterned biochemical signals to control cell behavior Adv *Adv. Mater* **27** 1356–62

[13] Gao Q, Niu X, Shao L, Zhou L, Lin Z, Sun A, Fu J, Chen Z, Hu J, Liu Y and He Y 2019 3D printing of complex GelMA-based scaffolds with nanoclay *Biofabrication* **11** 035006

[14] Ye D, Yang P, Lei X, Zhang D, Li L, Chang C, Sun P and Zhang L 2018 Robust anisotropic cellulose hydrogels fabricated via strong self-aggregation forces for cardiomyocytes unidirectional growth *Chem. Mater.* **30** 5175–83

[15] Kong W, Wang C, Jia C, Kuang Y, Pastel G, Chen C, Chen G, He S, Huang H, Zhang J, Wang S and Hu L 2018 Muscle-inspired highly anisotropic, strong, ion-conductive hydrogels *Adv. Mater.* **30** e1801934

[16] Vanaei S, Parizi M S, Vanaei S, Salemizadehparizi F and Vanaei H R 2021 An overview on materials and techniques in 3D bioprinting toward biomedical application *Engineered Regeneration* **2** 1–18

[17] Murphy S V and Atala A 2014 3D bioprinting of tissues and organs *Nat. Biotechnol.* **32** 773–85

[18] Daly A C, Prendergast M E, Hughes A J and Burdick J A 2021 Bioprinting for the biologist *Cell* **184** 18–32

[19] Munaz A, Vadivelu R K, St. John J, Barton M, Kamble H and Nguyen N-T 2016 Three-dimensional printing of biological matters *J. Sci. Adv. Mater. Devices* **1** 1–17

[20] Davidson C D, Jayco D K P, Matera D L, Depalma S J, Hiraki H L, Wang W Y and Baker B M 2020 Myofibroblast activation in synthetic fibrous matrices composed of dextran vinyl sulfone Acta Biomater *Acta Biomater*

[21] Guo Z, Dong L, Xia J, Mi S and Sun W 2021 3D Printing Unique Nanoclay‐Incorporated Double‐Network Hydrogels for Construction of Complex Tissue Engineering Scaffolds *Adv Healthcare Materials* **10**

[22] Si H, Xing T, Ding Y, Zhang H, Yin R and Zhang W 2019 3D bioprinting of the sustained drug release wound dressing with double-crosslinked hyaluronic-acid-based hydrogels *Polymers (Basel)* **11** 1584

[23] Nedunchezian S, Banerjee P, Lee C-Y, Lee S-S, Lin C-W, Wu C-W, Wu S-C, Chang J-K and Wang C-K 2021 Generating adipose stem cell-laden hyaluronic acid-based scaffolds using 3D bioprinting via the double crosslinked strategy for chondrogenesis *Mater. Sci. Eng. C Mater. Biol. Appl.* **124** 112072

[24] Bavaresco B, Comín R, Salvatierra N A and Cid M P 2020 Three-dimensional printing of collagen and hyaluronic acid scaffolds with dehydrothermal treatment crosslinking *Compos. Commun.* **19** 1–5

[25] Pan T, Song W, Xin H, Yu H, Wang H, Ma D, Cao X and Wang Y 2022 MicroRNA-activated hydrogel scaffold generated by 3D printing accelerates bone regeneration *Bioact. Mater.* **10** 1–14

[26] Nishiguchi A 2024 Advances in injectable hydrogels with biological and physicochemical functions for cell delivery *Polym. J.* **56** 895–903

[27] Liu H, Kitano S, Irie S, Levato R and Matsusaki M 2020 Collagen microfibers induce blood capillary orientation and open vascular lumen *Adv. Biosyst.* **4** e2000038

[28] Prendergast M E, Davidson M D and Burdick J A 2021 A biofabrication method to align cells within bioprinted photocrosslinkable and cell-degradable hydrogel constructs via embedded fibers *Biofabrication* **13**

[29] Kessel B, Lee M, Bonato A, Tinguely Y, Tosoratti E and Zenobi-Wong M 2020 3D bioprinting of macroporous materials based on entangled hydrogel microstrands *Adv. Sci. (Weinh.)* **7** 2001419

[30] Honkamäki L, Kulta O, Puistola P, Hopia K, Emeh P, Isosaari L, Mörö A and Narkilahti S 2025 Hyaluronic acid-based 3D bioprinted hydrogel structure for directed axonal guidance and modeling innervation in vitro *Adv. Healthc. Mater.* **14** e2402504

[31] Lee J, Lee H, Jin E-J, Ryu D and Kim G H 2023 3D bioprinting using a new photo-crosslinking method for muscle tissue restoration *npj Regenerative Medicine* **8** 1–14

[32] Liu H, Chansoria P, Delrot P, Angelidakis E, Rizzo R, Rutsche D, Applegate L A, Loterie D, Zenobi-Wong M and Light F 2022 FLight) Biofabrication of Highly Aligned Tissue-Engineered Constructs *Adv Mater* **34**

[33] Chan V, Zorlutuna P, Jeong J H, Kong H and Bashir R 2010 Three-dimensional photopatterning of hydrogels using stereolithography for long-term cell encapsulation *Lab Chip* **10** 2062–70

[34] Nishiguchi A, Ito S, Nagasaka K, Komatsu H, Uto K and Taguchi T 2024 Injectable microcapillary network hydrogels engineered by liquid-liquid phase separation for stem cell transplantation *Biomaterials* **305** 122451

[35] Nishiguchi A, Araki E, Palai D, Ito S and Taguchi T 2024 Development of Phase-Separating Microfiber Network Hydrogels to Promote In Vitro Vascularization *Biomacromolecules* **25** 6146–54

[36] Yasue H, Taguchi T, Asoh T-A and Nishiguchi A 2025 Cell‐delivering injectable hydrogels with tunable microporous structures improve therapeutic efficacy for volumetric muscle loss *Adv. Funct. Mater.*

[37] Shirahama H, Lee B H, Tan L P and Cho N-J 2016 Precise tuning of facile one-pot gelatin methacryloyl (GelMA) synthesis *Sci. Rep.* **6** 31036

[38] Nishiguchi A, Ichimaru H, Ito S, Nagasaka K and Taguchi T 2022 Hotmelt tissue adhesive with supramolecularly-controlled sol-gel transition for preventing postoperative abdominal adhesion *Acta Biomater.* **146** 80–93

[39] Ouyang L, Armstrong J P K, Lin Y, Wojciechowski J P, Lee-Reeves C, Hachim D, Zhou K, Burdick J A and Stevens M M 2020 Expanding and optimizing 3D bioprinting capabilities using complementary network bioinks *Science Advances* **6** eabc5529

[40] Caprio N D, Davidson M D, Daly A C and Burdick J A 2024 Injectable MSC spheroid and microgel granular composites for engineering tissue *Adv. Mater.* **36** e2312226

[41] Wang Q, Karadas Ö, Rosenholm J M, Xu C, Näreoja T and Wang X 2024 Bioprinting macroporous hydrogel with aqueous two‐phase emulsion‐based bioink: In vitro mineralization and differentiation empowered by phosphorylated cellulose nanofibrils *Adv. Funct. Mater.* **34**

[42] Shao L, Jiang J, Yuan C, Zhang X, Gu L and Wang X 2024 Omnidirectional anisotropic embedded 3D bioprinting Mater Today Bio 27 101160 **27**

[43] Folkman J and Hochberg M 1973 Self-regulation of growth in three dimensions *J. Exp. Med.* **138** 745–53

[44] Thomas D, O'brien T and Pandit A 2018 Toward customized extracellular niche engineering: Progress in cell-entrapment technologies Adv *Adv. Mater* **30**

[45] Denes L T, Riley L A, Mijares J R, Arboleda J D, McKee K, Esser K A and Wang E T 2019 Culturing C2C12 myotubes on micromolded gelatin hydrogels accelerates myotube maturation *Skelet. Muscle* **9** 17

[46] Hosseini V, Ahadian S, Ostrovidov S, Camci-Unal G, Chen S, Kaji H, Ramalingam M and Khademhosseini A 2012 Engineered contractile skeletal

muscle tissue on a microgrooved methacrylated gelatin substrate *Tissue Eng. Part A* **18** 2453–65

[47] Galipeau J and Sensébé L 2018 Mesenchymal stromal cells: Clinical challenges and therapeutic opportunities *Cell Stem Cell* **22** 824–33